Dynamics of Atmospheres and Oceans 98 (2022) 101288

Contents lists available at ScienceDirect

Dynamics of Atmospheres and Oceans

journal homepage: www.elsevier.com/locate/dynatmoce

Opposite responses of sea level variations to ENSO in the Northwestern Pacific: A transition latitude at 20°N

Haihong Guo [a,b], Zhaohui Chen [a,b,*], Jia-Zhen Wang [a,b], Haiyuan Yang [a,b]

[a] Frontier Science Center for Deep Ocean Multispheres and Earth System (FDOMES) and Physical Oceanography Laboratory, Ocean University of China, Qingdao, China
[b] Qingdao National Laboratory for Marine Science and Technology, Qingdao, China

ARTICLE INFO

Keywords:
Sea level
Interannual variations
ENSO
Matsuno-Gill response
Hadley Cell

ABSTRACT

The interannual sea level variations in the Northwestern Pacific are significantly tied to the El Niño-Southern Oscillation (ENSO), with opposite responses and asymmetric strength to the south and north of 20°N. Using a 1.5-layer reduced gravity model, we show that the spatial pattern of sea level interannual variations is not sensitive to the existence of the Luzon Strait located at around 20°N, but is dominated by the basin-scale wind stress curl associated with ENSO. Dynamically, sea level variations tied to ENSO are attributed to long baroclinic Rossby wave adjustment driven by wind stress curl in the western/central Pacific, as previous studies have indicated. However, the responses of wind stress curl to ENSO are dynamically different to the south and north of 20°N. In the tropics, the wind stress curl anomaly results from the ENSO event directly, through the Matsuno-Gill response with the transition of zonal wind anomaly at approximately 20°N, while in the subtropics, the wind stress curl anomaly is mainly set up by atmospheric vertical motions through the Hadley Cell.

1. Introduction

The sea level change has always been a hot topic in recent decades, whose global and regional variability has received much attention from a variety of studies (Church and White, 2006; Vermeer and Rahmstorf, 2009; Marcos et al., 2012; Qiu and Chen, 2012; Stammer et al., 2013; Qiu et al., 2015), particularly after the launch of satellite altimetry in the early 1990s (Chelton and Schlax, 1996; Cazenave et al., 1997; Criado-Aldeanueva et al., 2008; Ablain et al., 2015;). In the tropical western Pacific Ocean, the sea level has experienced prominent rising with the trend over 10 mm yr^{-1} in the past two decades, which is three times faster than the global mean (Qiu and Chen, 2012). They attributed this accelerating sea level rise to upper-ocean water mass redistribution caused by the surface wind stresses of the recently strengthened atmospheric Walker circulation (Qiu and Chen, 2012).

An interesting feature of the recent long-term sea level rise in the Northwestern Pacific (NWP) is the regionally enhanced rising signals appear to be confined to the south of 20°N, while less prominent sea level change is identified to its north (Fig. 1 in Qiu and Chen, 2012). This rising trend of sea level continues as we extend the observation period to 2019 (figure not shown). Interestingly, the transition is also remarkable as we only focus on the interannual sea surface height (SSH) variations. On interannual timescales, the well-known dominant mode of the SSH is characterized by a zonal pattern in the tropical western Pacific versus eastern Pacific. As

* Corresponding author at: Frontier Science Center for Deep Ocean Multispheres and Earth System (FDOMES) and Physical Oceanography Laboratory, Ocean University of China, Qingdao, China.
E-mail address: chenzhaohui@ouc.edu.cn (Z. Chen).

https://doi.org/10.1016/j.dynatmoce.2022.101288
Received 29 July 2021; Received in revised form 8 February 2022; Accepted 24 February 2022
Available online 26 February 2022

shown in Fig. 1a, the leading variations of the observed SSH derived from empirical orthogonal function (EOF) analysis show a transition band at approximately 20°N, which seems to 'block' the tropical SSH signals from extending further north. The 1st principal component (PC-1) with 56% variance contribution rate highly correlates with the Oceanic Niño Index (ONI) (Fig. 1b) with the coefficient reaching over 0.8. In the subtropics, contrastingly, the SSH signals are weak and reversed from the tropical counterpart (Fig. 1a). Hence, it is speculated that the El Niño-Southern Oscillation (ENSO), the dominating interannual sea surface temperature (SST) signals in the tropical Pacific, exerts quite remarkable remote impacts with opposite SSH variations in the subtropical and tropical North Pacific.

As we focus on the tropical western Pacific, the SSH heaps up (down) between the Philippine coast and the dateline during La Niña (El Niño) years centering at approximately 10°N (Fig. 1a). The SSH signals gradually weaken towards the north and reverse at the transition latitude of about 20°N where the Luzon Strait (LS) locates. Dynamically, SSH signals generated by wind forcing propagate westward through baroclinic Rossby waves off the equator until encountering the western boundary, so the ENSO-related signals may travel across the LS and leak into the northern SCS. As an interchange of water and heat between the SCS and the Pacific (Qu et al., 2004), the LS may provide a pathway for SSH signals from the Pacific to the SCS (Zheng et al., 2011; Xiu et al., 2010). It is speculated that the LS may serve as a gap that leaks SSH signals responding to ENSO, and probably conveys ENSO impacts into the SCS (Qu et al., 2004). Another candidate accounting for the SSH pattern may arise from the basin-scale wind forcing, which can excite low-frequency SSH anomalies through Rossby waves in the western-central Pacific (Qiu and Chen, 2010).

To verify the role of potential factors that control the SSH pattern, we used a 1.5–layer reduced gravity model in conjunction with analyzing a set of observation/reanalysis data. The rest of this study is organized as follows. After describing the datasets and model in Section 2, we present the sensitive experiment results in Section 3. The role of wind forcing tied to ENSO is presented in Section 4, by elucidating its dynamical link with local processes and the Hadley Cell. Section 5 summarizes the results.

2. Data and methods

The data used in this study include monthly mean SSH, surface wind stresses, and three-dimensional winds on pressure levels. The Ssalto/Duacs altimeter products (1993–2019) were produced and distributed by the Copernicus Marine and Environment Monitoring Service (CMEMS) (http://www.marine.copernicus.eu). The monthly surface wind stresses from European Centre for Medium-Range Weather Forecasts (ECMWF) ERA5 reanalysis (Hersbach et al., 2019a) are used to force the 1.5-layer reduced gravity model. The monthly horizontal and vertical velocities from the ERA5 reanalysis (Hersbach et al., 2019b) are also used to depict the three-dimensional structure of the circulation variations. The Oceanic Niño Index (ONI) is the 3-month running mean of the SST anomalies from Extended Reconstructed Sea Surface Temperature (ERSSTv5) in the Niño 3.4 region (5°N to 5°S, 120°W to 170°W) (Huang et al., 2017). In addition, the surface wind stresses used for intercomparisons are derived from seven reanalysis datasets including the ERA5, the Cross-Calibrated Multi-Platform (CCMP) (Mears et al., 2019), the Japanese 55-year Reanalysis (JRA-55)

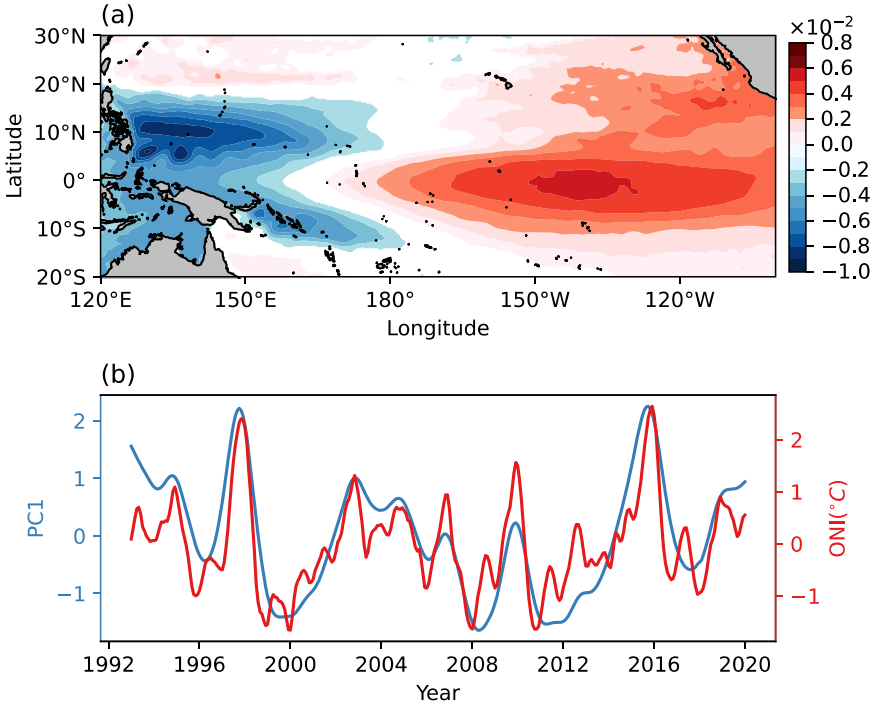

Fig. 1. (a) The EOF mode-1 of altimetry-observed SSH in the low-latitude Pacific (20°S to 30°N). The linear trend and seasonal cycle have been removed before the EOF analysis. (b) The normalized PC-1 (blue) and ONI (red) derived from ERSSTv5.

(Kobayashi et al., 2015), the Modern-Era Retrospective Analysis for Research and Applications version 2 (MERRA-2) (Gelaro et al., 2017), the NCEP Climate Forecast System Reanalysis (CFSR) (Saha et al., 2010), the NCEP/NCAR 40-Year Reanalysis (Kalnay et al., 1996), and the NCEP reanalysis 2 (Kanamitsu et al., 2002). Detailed descriptions for these datasets are provided in Table 1.

In this study, numerical simulations are performed using a 1.5–layer reduced gravity model following Chen and Wu (2011). The governing equations for this model are as follows:

$$\frac{\partial u}{\partial t}+u\frac{\partial u}{\partial x}+v\frac{\partial u}{\partial y}-fv+g'\frac{\partial h}{\partial x}=A_H\nabla^2 u+\frac{\tau^x}{\rho(h+H)} \tag{1a}$$

$$\frac{\partial v}{\partial t}+u\frac{\partial v}{\partial x}+v\frac{\partial v}{\partial y}+fu+g'\frac{\partial h}{\partial y}=A_H\nabla^2 v+\frac{\tau^y}{\rho(h+H)} \tag{1b}$$

$$\frac{\partial h}{\partial t}+\frac{\partial hu}{\partial x}+\frac{\partial hv}{\partial y}=0 \tag{1c}$$

where u and v denote the zonal and meridional velocity, h is the perturbation from the mean upper layer thickness H, A_H is the lateral eddy viscosity, τ^x and τ^y represent the zonal and meridional wind stresses, and ρ is the reference density (1025 kg m^{-3}). The density contrast ($\Delta\rho$) between the abyssal ocean and the upper-layer ocean is set to 3.2 kg m^{-3} and the gravity parameter g is 9.81 m s^{-2}. Therefore, the reduced gravity acceleration g' is 0.031 m s^{-2}, based on which the calculated phase speed of internal gravity waves is consistent with the background value in the low-latitude Pacific.

The model is configured in a closed domain (100°E to 70°W, 40°S to 45°N) with the horizontal resolution of 0.25°. Marginal seas shallower than 600 m are treated as land, and all islands in the ocean interior are removed. The initial thickness of the upper layer is $H = 400$ m. No normal flow and no-slip boundary conditions are employed along the lateral boundaries. Note that the Indonesian Throughflow (ITF), the key passage connecting the Pacific and the Indian Ocean, has been removed in all model tests since the results are not sensitive to the absence of the ITF. There is increased lateral eddy viscosity within the 10° latitudes band near the northern and southern boundary to suppress the suspicious boundary-trapped Kelvin waves generated in the model. Although the increased viscosity cannot fully damp all the boundary-trapped Kelvin waves, these signals have insignificant influences on the low-latitude ocean circulation. Thus, the results from the model between 20°S and 30°N will be analyzed subsequently.

3. Model results

The 1.5-layer reduced gravity model reached a steady state after a 30-year integration forced by the climatological wind stress from ERA5. After that, the model was restarted based on the mean fields of the last 5 years' integration and was forced by the monthly wind stress from 1979 to 2020 (standard run). To accommodate the altimeter observation period, the simulated SSH (calculated as $\eta = h\Delta\rho/\rho$) from 1993 to 2019 was used for analysis.

The EOF analysis is conducted using the modeled SSH anomaly (SSHa) (Fig. 2). Despite its idealization and simplicity, the model-simulated interannual variations of SSHa are in good agreement with observations in terms of the temporal and spatial pattern. Most importantly, the 1.5-layer reduced gravity model reasonably captures the transition latitude of the SSH interannual variability. The correlation between the modeled SSH PC-1 and ONI is 0.81 above the 95% level of significance, indicating again the capability of the simple model in reproducing the spatial pattern of SSH interannual variability.

The consistency between model and observations provides a practical way to test the potential role of LS and wind forcing. Further diagnostic runs are needed to test these potential contributions. First, to highlight the role of LS, we designed a model test in which the LS is completed blocked (non-LS run), while everything else in the model remains identical to the standard run.

Despite the shutdown of the exchange between the NWP and SCS, there seems to be no evident difference in the interannual SSH variations between the non-LS run and standard run (Fig. 2). The correlation coefficient between the PC-1 from the modeled SSH in the non-LS run and the ONI is 0.80 above the 95% level of significance, which is nearly identical to that in the standard run. In this regard, the existence of the LS does not essentially affect the SSH pattern, indicating that the shape of western boundary play minor roles. Physically, the gap-leaping Kuroshio actually provides a strong cross-stream potential vorticity (PV) gradient that blocks the westward

Table 1
Datasets used in this study.

Dataset	Variable	Horizontal resolution	Time span
CMEMS	SSH	0.25° × 0.25°	1993–2019
ERA5	Surface wind stress	0.25° × 0.25°	1979–2020
ERA5	3D wind velocities	0.25° × 0.25°	1993–2019
ERSSTv5	ONI	————	1993–2019
CCMP	Surface wind stress	0.25° × 0.25°	1993–2019
JRA-55	Surface wind stress	1.25° × 1.25°	1993–2019
MERRA-2	Surface wind stress	0.5° × 0.625°	1993–2019
CFSR	Surface wind stress	0.5° × 0.5°	1993–2019
NCEP1	Surface wind stress	2.5° × 2.5°	1993–2019
NCEP2	Surface wind stress	2.5° × 2.5°	1993–2019

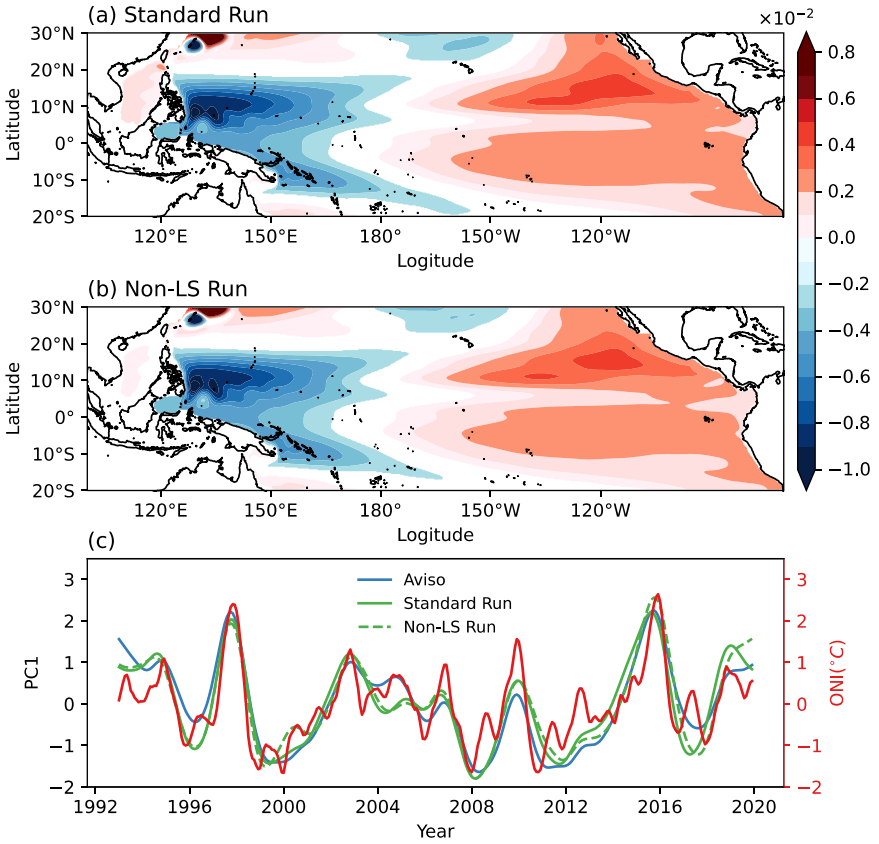

Fig. 2. The EOF mode-1 of SSH between 20°S and 30°N for (a) the standard run and (b) the non-LS run in the 1.5-layer reduced gravity model. (b) The PC-1 time series of the observed SSH (solid blue), the standard run (solid green), and the non-LS run (dashed green). The red line denotes the ONI.

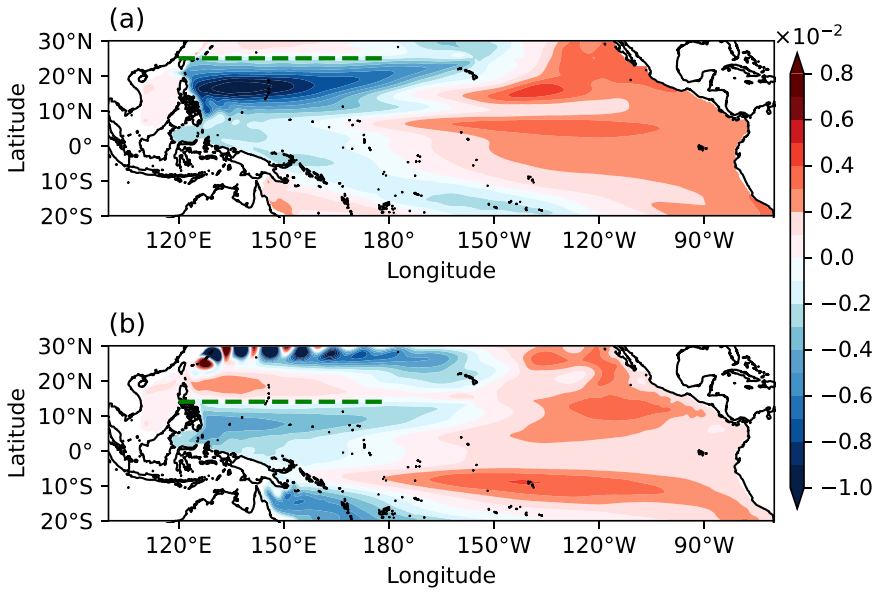

Fig. 3. The EOF mode-1 of SSH between 20°S and 30°N for the cases where the wind stress of the whole basin was moved 5° northward (a) and 5° southward (b).

propagation of Rossby waves (Lu and Liu, 2013), and this is also the case for the numerical model simulations.

It has been previously discussed that the low-latitude upper ocean variability is effectively controlled by local wind forcing and remotely propagating baroclinic Rossby waves in both observational and modeling approaches (e.g., Chelton and Schlax, 1996; Qiu and Chen, 2010; Chen et al., 2014). Additional model runs with northward/southward shift of wind stress have been carried out. Not surprisingly, as shown in Fig. 3, the transition latitude of SSH follows the wind stress closely, which shifts northward (Fig. 3a) and southward (Fig. 3b) as we artificially change the spatial pattern of wind field in the model.

We also performed two tests to examine the contributions of local (west of 140°E) wind forcing and remote Rossby waves. For the case where the local wind stress was fixed, that is, the time-varying wind stress is replaced by time-mean wind stress, and the modeled SSH shows a similar structure to the standard run. On the contrary, the observed SSH pattern in the western Pacific cannot be reproduced as we fixed the remote wind forcing (not shown). The above model tests explicitly demonstrate that the observed SSH pattern, particularly for the SSH transition latitude at 20°N, is not attributed to the special geographic features, but to the wind stress forcing from the remote Pacific.

4. Role of winds tied to ENSO

To examine the role of wind forcing in explaining the SSH pattern at interannual time scales, a lead-lag correlation between the SSH and wind forcing is conducted. As shown in Fig. 4, there is a key region that correlates well with the PC-1 of the observed SSH in the tropical western Pacific (10–20°N, 140–170°E). Further examination indicates the correlation reaches its maximum when the wind stress curl in the key region leads the PC-1 by about 4 months, with the correlation coefficient ranging from 0.78 to 0.92 as seen from a variety of wind products (Fig. 4b). This implies that the SSH pattern is predominantly controlled by the wind stress curl in the western and central Pacific, consistent with the conclusions of previous studies (Qiu and Chen, 2010; Hu et al., 2016). Another issue that should be addressed here is the correlation map exhibits a clear transitioning latitude at around 20°N as well (Fig. 4a), quite similar to the SSH pattern shown above.

The wind stress curl, as shown in Fig. 5, acts as an atmosphere agent in linking the SSH and ENSO (Qiu and Lukas, 1996; Qiu and Chen, 2010; Wang et al., 2020) since the regression of wind stress curl onto the ONI is quite similar to the correlation map (Fig. 4). The composite wind stress curl shows a positive (negative) anomaly to the south of 20°N during the El Niño (La Niña) event when the wind stress curl leads the ONI index by 4 months (Fig. 5b, d). This positive (negative) wind stress curl produces oceanic upwelling (downwelling) westward propagating baroclinic Rossby waves, which drops (lifts) the SSH as they encounter the western Pacific. In contrast, the response of wind stress curl to the ENSO in the subtropics is quite different from that in the tropics. In the subtropics, the ENSO-induced wind stress curl anomaly is centered at the dateline and lags the ONI by about 3 months (Fig. 5c, e), which excites opposite Rossby waves compared to the tropics.

Moreover, the latitude dependence of baroclinic Rossby wave speed may also lead to different responses in tropics and subtropics.

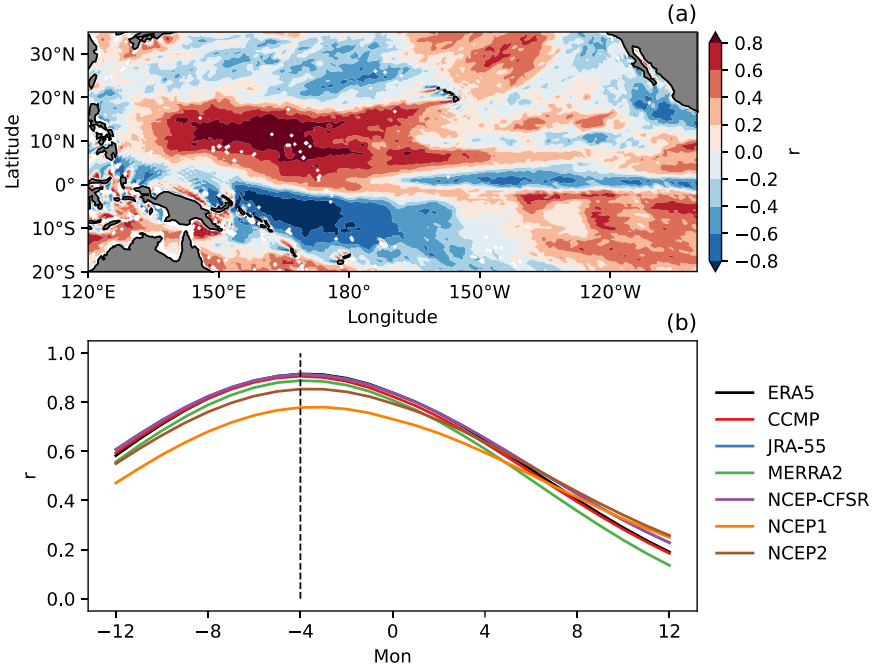

Fig. 4. (a) Correlation map when the wind stress curl from ERA5 leads the PC-1 of observed SSH by 4 months. (b) The lead-lag correlation coefficient between the wind stress curl from multiple-products averaged within a box of 10–20°N and 140–170°E and the PC-1 of observed SSH. The solid lines denote the correlation coefficient is over the 95% confidence level.

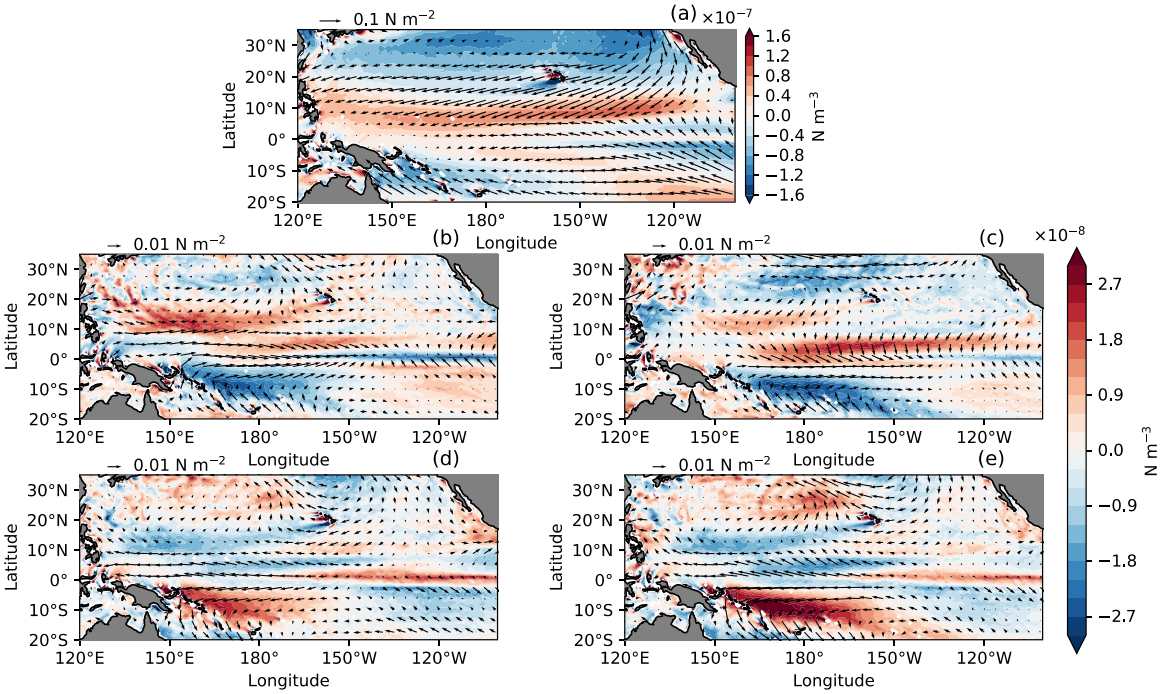

Fig. 5. (a) Climatology wind stress curl (color shading) and wind vector (arrow). Composite wind stress curl anomaly and wind vector as the winds lead ONI by 4 months during (b) El Niño and (d) La Niña events, and lag ONI by 3 months during (c) El Niño and (e) La Niña events.

In the tropics, the accumulating SSH is not sensitive to Rossby wave speeds as we focus on the interannual variability. For example, at 15°N, the first baroclinic Rossby wave speed is around 0.15 m/s. It takes around 5 months for these waves to propagate from the key region (140–170°E) to the western Pacific. Given that the Rossby waves run faster in the lower latitude, the traversing time of the Rossby wave in the tropics is much smaller than the ENSO period (2–7 years). However, in the subtropical Pacific, the traversing time of the Rossby waves is comparable to some of ENSO events. The first baroclinic Rossby wave speed at 25°N is 0.05 m/s, which results in a 3–4-year traveling timescale from the dateline to the western boundary region. This may account for the weak manifestation of SSH interannual variability in the subtropical Pacific.

Therefore, it is the opposite and asynchronous responses of wind stress curl in the tropical and subtropical North Pacific that account for the meridional contrast in SSH pattern. The dynamics of the tropical wind stress curl is quite different from that in the subtropics. In the tropics, the wind stress curl anomaly is explained by the Matsuno-Gill model in response to the SST anomaly. In the

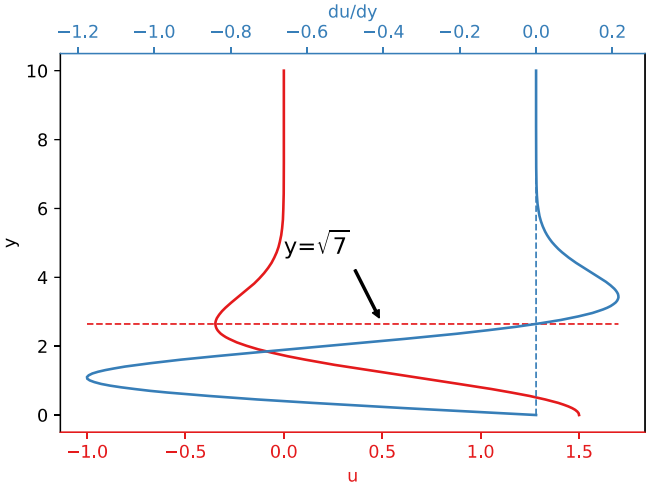

Fig. 6. The nondimensional zonal velocity (solid red) and its meridional gradient (solid blue) as a function of nondimensional distance (y) from the equator. The dimensional unit length scale of y is approximately 1000 km so that the zero line of zonal velocity (dashed red), where $y = \sqrt{7}$, corresponds to 2600 km in the dimensional form. In this case $q_2(x) = -1$.

subtropics, the main agent that links the ENSO-induced SST with the resultant wind stress curl is the basin-scale atmospheric circulation, i.e., the Hadley Cell, which is characterized by an overturning atmospheric circulation driven by the latitudinal heating gradient.

In the tropical Pacific, the positive SST anomalies during the El Niño event produce a pair of cyclones in the off-equatorial region (Gill, 1980), which features westerly anomalies on the equator. This westerly wind falls to zero away from the equator, with weak easterly wind further developing on the poleward edge of the cyclones. To verify the meridional extent of the tropical response, we use the classical Matsuno-Gill model to evaluate the meridional scale of the anomalous cyclones. Following Gill (1980), the non-dimensional solution of the zonal velocity u is:

$$u = \frac{1}{2} q_2(x)\left(y^2 - 3\right)\exp\left(-\frac{1}{4}y^2\right) \tag{2}$$

where x and y are the nondimensional distance with the positive direction pointing eastward and northward from the equator, respectively, both of which are scaled by the equatorial Rossby deformation radius $\sqrt{c/2\beta}$, $q_2(x)$ is an expansion depending only on the x coordinate. Physically, the parameter c is the phase speed of the first baroclinic gravity wave, which is around 50 m/s for the equatorial atmosphere (Li and Hsu, 2018). Therefore, the dimensional unit length scale is around 1000 km.

In the North Pacific, the wind stress curl is primarily dominated by the meridional shear of the zonal wind stress. Therefore, the northern edge of the anomaly wind stress curl off the equator is located at the latitude where the easterly wind stress reaches its

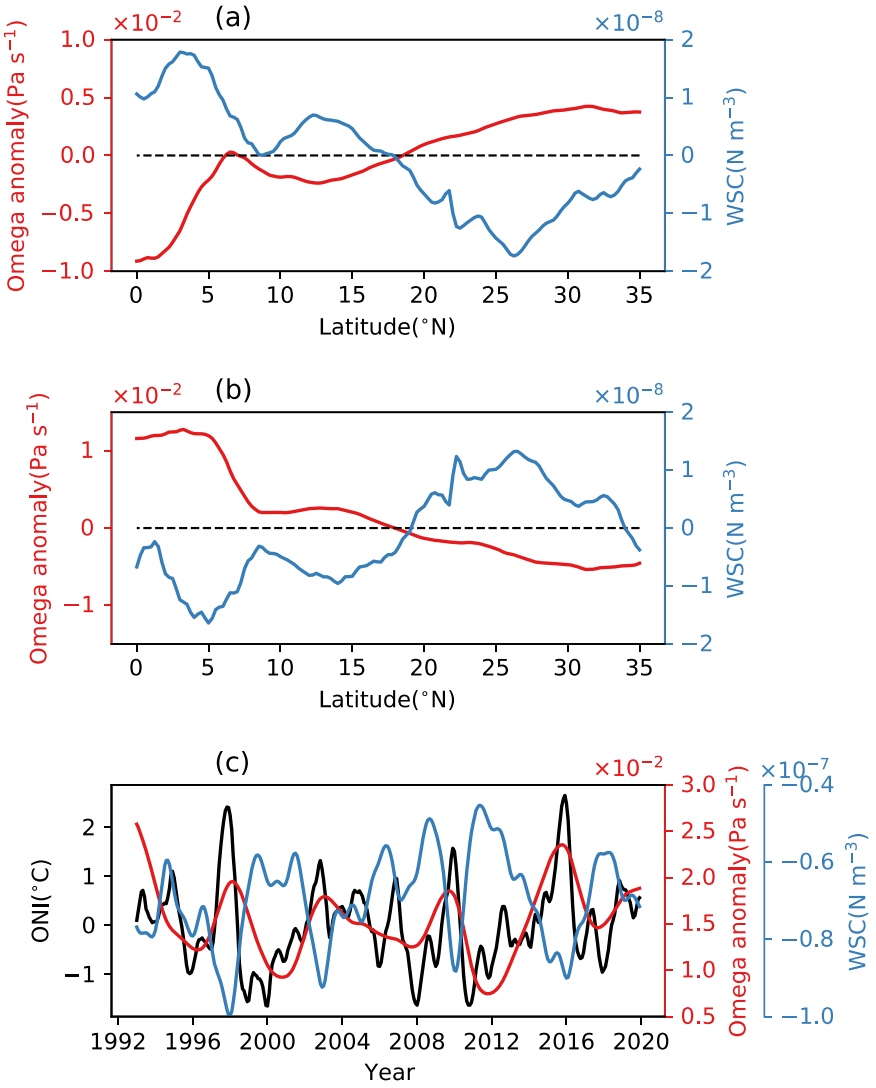

Fig. 7. The composite vertical velocity anomaly and wind stress curl anomaly when the wind lags the ONI by 3 months during the El Niño (a) and La Niña (b) event. (c), The 2-year low-passed vertical velocity and wind stress curl averaged in the 20–30°N and 160°E to 160°W box, and ONI index.

maximum (Fig. 6), which can be simply obtained from $du/dy = 0$. Since $q_2(x)$ is negative (Gill, 1980) and is not a function of y, we choose $q_2(x) = -1$ for simplicity. It is easy to verify from Eq. (2) that the meridional derivative of the zonal velocity drops to zero at $y = \sqrt{7}$, corresponding to the dimensional length scale of about 2600 km. Considering that the Matsuno-Gill model uses an equatorial beta-plane approximation that gives a constant Rossby deformation radius, while realistically the Rossby deformation radius decreases towards higher latitudes, so the theoretical meridional scale of the tropical wind stress curl anomaly is overestimated base on equatorial beta-plane approximation. It has been validated in many works by using simple atmospheric models (see Fig. 7 in Zebiak, 1982), simple atmosphere-ocean coupled models (Fig. 7 in Zebiak and Cane, 1987;), and complex models (e.g., Fig. 17 in Kiladis et al., 2009) that the easterly wind anomaly peaks at around 20°N, which is generally consistent with the realistic wind stress curl anomaly in response to ENSO-related SST (Fig. 5).

In the subtropics, however, the responses of the wind stress curl to the ENSO event are related to the variation of Hadley Cell, which is quite different from the tropics. At interannual timescales, the Hadley Cell is believed to be closely linked with ENSO (Ma and Li, 2008; Nguyen et al., 2013), particularly during the mature phase of El Niño events (Stachnik and Schumacher, 2011). Climatically, the North Pacific subtropical gyre is bounded by the zero line of the wind stress curl at around 15°N, which is the southern edge of the Hadley Cell downward motion. However, the transition latitude of the interannual wind stress curl anomaly is located at a higher latitude rather than the zero line of the mean state. Based on the correlation map (Fig. 4a), the opposite correlation is located to the north of 20°N. To quantitatively describe the possible link between wind stress curl in the subtropical central Pacific and ENSO, we choose the vertical velocity averaged in the 20–30°N and 160°E to 160°W box to represent the local Hadley Cell strength.

It is shown in Fig. 7c that the correlation between ONI and velocity of vertical motions reaches a maximum (0.63) when the velocity lags the ONI by approximately 3 months. The contemporaneous correlation between vertical motion and wind stress curl is − 0.68. Therefore, the interannual variations of subtropical wind stress curl lag those of the tropics by 7 months (Fig. 5). As the wind lags ONI by 3 months, the composite vertical velocity anomaly and wind stress curl anomaly averaged in the 160°E to 160°W band intersect at around 20°N and reverse from the south to north of this latitude (Fig. 7a, b). Although the transition latitude somewhat shifts southward during the El Niño event, it is still located to the north of the zero line of the local wind stress curl (10°N, not shown). Therefore, the meridional scale of the mean state wind stress curl is dynamically different from the response of its anomaly induced by the ENSO event.

During the El Niño (La Niña) event, the strengthening (weakening) of the Hadley Cell enhances (weakens) the exchange between the tropics and subtropics. An atmospheric upward (downward) motion leads to a convergence (divergence) of surface winds, which generates a positive (negative) wind stress curl in the Northern Hemisphere. Therefore, the anomalous Hadley Cell leads to a downward (upward) atmospheric motion anomaly in the subtropical North Pacific near the dateline, giving rise to negative (positive) wind stress curl locally (Fig. 5c, e).

To summarize, the tropical wind stress curl anomaly is owing to the Matsuno-Gill pattern in response to SST anomaly during ENSO, while the meridional Hadley Cell determines the wind stress curl variations in the remote subtropics. It should be noted that the broad-scale upward/downward motion is demarcated by a certain band at 20°N in the central North Pacific, consistent with the resultant SSH pattern driven by the wind stress curl.

5. Summary and discussion

In this study, we investigated the interannual variability of SSH in the NWP and its transition latitude at approximately 20°N. The SSH in the tropical NWP drops (rises) during the El Niño (La Niña) periods. However, this strong pattern is only limited in the low-latitude to the south of 20°N and it shows an opposite but relatively weak signal in the subtropics compared to the tropics. It is interesting that the transition latitude is not attributed to the existence of the Luzon Strait according to our numerical model tests using a 1.5-layer reduced gravity model.

Further analysis on the relationship between the SSH and wind stress curl suggested that it is the ENSO-induced wind stress curl anomaly that produces the SSH pattern with a transition at around 20°N. This transition latitude is quite different from the zero line of the background wind stress curl. In the tropics, the meridional scale of wind stress curl anomaly is determined by the Matsuno-Gill response with an off-equator cyclone (anticyclone) bounded at around 20°N during El Niño (La Niña) event. In the subtropics, the variations of wind stress curl anomaly can be attributed to the local Hadley Cell response to the ENSO with negative (positive) wind stress curl north of 20°N during El Niño (La Niña) event.

Although there have been numerous studies that revealed the ENSO-related oceanic response in the NWP, this work provides a concise image describing the relationship between the ENSO and spatial pattern of SSH. The transition latitude of interannual SSH is determined by the asynchronous surface wind variations in the tropics and subtropics owing to the Gill pattern and local Hadley Cell, respectively. It can be acceptable that the remote wind forcing mechanism is not the only possible factor that influences the dynamics of SSH variations in the NWP. The decreasing (increasing) SSH trend south (north) of the Subtropical Countercurrent caused by the decadal weakening of the regional eddy momentum flux forcing (Qiu et al., 2015), and local Asian Monsoon variability (Yaremchuk and Qu, 2004) are all likely to be important candidates in governing water mass redistribution between the tropical and subtropical NWP. Thus, the contribution of these factors in explaining the SSH response at different timescales should be addressed in future modeling studies.

CRediT authorship contribution statement

Haihong Guo: formulation or evolution of overarching research goals and aims; creation of models; writing the initial draft. **Zhaohui Chen:** Ideas; Management and coordination responsibility for the research activity planning and execution; Acquisition of the financial support for the project leading to this publication. **Jia-Zhen Wang:** Conducting a research and investigation process; critical review. **Haiyuan Yang:** Development or design of methodology.

Declaration of Competing Interest

The authors declare that they have no known competing financial interests or personal relationships that could have appeared to influence the work reported in this paper.

Acknowledgments

This research is funded by National Natural Science Foundation of China (42076009 and 41806008), the China Scholarship Council (201906330102) and Qingdao Pilot National Laboratory for Marine Science and Technology (2017ASTCP-ES05). Z. C. is partially supported by Taishan Scholar Funds (tsqn201812022) and Fundamental Research Funds for the Central Universities (202072001). Data used here are publicly available from: CMEMS (http://www.marine.copernicus.eu), ERA5 (the Copernicus Climate Change Service Climate Data Store https://cds.climate.copernicus.eu/), ONI (https://origin.cpc.ncep.noaa.gov/products/analysis_monitoring/ensostuff/ONI_v5.php), CCMP (www.remss.com/measurements/ccmp), JRA-55 (http://rda.ucar.edu/datasets/ds628.1/), MERRA-2 (https://disc.gsfc.nasa.gov/datasets?project=MERRA-2), NCEP-CFSR (https://climatedataguide.ucar.edu/climate-data/climate-forecast-system-reanalysis-cfsr.), NCEP1 (https://psl.noaa.gov/data/gridded/data.ncep.reanalysis.html), NCEP2 (http://www.cpc.ncep.noaa.gov/products/wesley/reanalysis2/kana/reanl2-1.htm).

References

Ablain, M., et al., 2015. Improved sea level record over the satellite altimetry era (1993–2010) from the climate change initiative project. Ocean Sci. 11, 67–82. https://doi.org/10.5194/os-11-67-2015.

Cazenave, A., Bonnefond, P., Dominh, K., Schaeffer, P., 1997. Caspian sea level from Topex-Poseidon altimetry: level now falling. Geophys. Res. Lett. 24, 881–884. https://doi.org/10.1029/97GL00809.

Chelton, D.B., Schlax, M.G., 1996. Global observations of oceanic Rossby waves. Science (80-) 272, 234–238. https://doi.org/10.1126/science.272.5259.234.

Chen, Z., Wu, L., 2011. Dynamics of the seasonal variation of the north equatorial current bifurcation. J. Geophys. Res. 116, C02018 https://doi.org/10.1029/2010JC006664.

Chen, Z., Wu, L., Qiu, B., Sun, S., Jia, F., 2014. Seasonal variation of the south equatorial current bifurcation off Madagascar. J. Phys. Oceanogr. 44, 618–631. https://doi.org/10.1175/JPO-D-13-0147.1.

Church, J.A., White, N.J., 2006. A 20th century acceleration in global sea-level rise. Geophys. Res. Lett. 33 https://doi.org/10.1029/2005GL024826.

Criado-Aldeanueva, F., Del Río Vera, J., García-Lafuente, J., 2008. Steric and mass-induced Mediterranean sea level trends from 14 years of altimetry data. Glob. Planet. Change 60, 563–575. https://doi.org/10.1016/j.gloplacha.2007.07.003.

Gelaro, R., et al., 2017. The modern-era retrospective analysis for research and applications, version 2 (MERRA-2). J. Clim. 30, 5419–5454. https://doi.org/10.1175/JCLI-D-16-0758.1.

Gill, A., 1980. Some simple solutions for heat-induced tropical circulation. Q. J. R. Meteorol. Soc. 106, 447–462. https://doi.org/10.1256/smsqj.44904.

Hersbach, H., et al., 2019a. ERA5 monthly averaged data on single levels from 1979 to present. Copernicus Climate Change Service (C3S) Climate Data Store (CDS). ⟨https://doi.org/10.24381/cds.f17050d7⟩, (Accessed 20 January 2020).

Hersbach, H., et al., 2019a. ERA5 monthly averaged data on pressure levels from 1979 to present. Copernicus Climate Change Service (C3S) Climate Data Store (CDS). ⟨https://doi.org/10.24381/cds.6860a573⟩, (Accessed 20 January 2020).

Hu, S., Hu, D., Guan, C., Wang, F., Zhang, L., Wang, F., Wang, Q., 2016. Interannual variability of the mindanao current/undercurrent in direct observations and numerical simulations. J. Phys. Oceanogr. 46, 483–499. https://doi.org/10.1175/JPO-D-15-0092.1.

Huang, B., et al., 2017. Extended reconstructed Sea surface temperature, Version 5 (ERSSTv5): upgrades, validations, and intercomparisons. J. Clim. 30, 8179–8205. https://doi.org/10.1175/JCLI-D-16-0836.1.

Kalnay, E., et al., 1996. The NCEP/NCAR 40-year reanalysis project. Bull. Am. Meteorol. Soc. 77, 437–472. https://doi.org/10.1175/1520-0477(1996)077<0437:TNYRP>2.0.CO;2.

Kanamitsu, M., Ebisuzaki, W., Woollen, J., Yang, S.-K., Hnilo, J.J., Fiorino, M., Potter, G.L., 2002. NCEP–DOE AMIP-II reanalysis (R-2). Bull. Am. Meteorol. Soc. 83, 1631–1644. https://doi.org/10.1175/BAMS-83-11-1631.

Kiladis, G.N., Wheeler, M.C., Haertel, P.T., Straub, K.H., Roundy, P.E., 2009. Convectively coupled equatorial waves. Rev. Geophys. 47, 1–42. https://doi.org/10.1029/2008RG000266.

Kobayashi, S., et al., 2015. The JRA-55 reanalysis: general specifications and basic characteristics. J. Meteorol. Soc. Jpn. 93, 5–48. https://doi.org/10.2151/jmsj.2015-001.

Li, T., Hsu, P., 2018. Simple Dynamic Frameworks for Tropical Atmosphere and Ocean. Fundamentals of Tropical Climate Dynamics, pp. 1–40. ⟨https://link.springer.com/book/10.1007%2F978-3-319-59597-9⟩.

Lu, J., Liu, Q., 2013. Gap-leaping Kuroshio and blocking westward-propagating Rossby wave and eddy in the Luzon Strait. J. Geophys. Res. Oceans 118, 1170–1181. https://doi.org/10.1002/jgrc.20116.

Ma, J., Li, J., 2008. The principal modes of variability of the boreal winter Hadley cell. Geophys. Res. Lett. 35, 1–5. https://doi.org/10.1029/2007GL031883.

Marcos, M., Tsimplis, M.N., Calafat, F.M., 2012. Inter-annual and decadal sea level variations in the north-western Pacific marginal seas. Prog. Oceanogr. 105, 4–21. https://doi.org/10.1016/j.pocean.2012.04.010.

Mears, C.A., Scott, J., Wentz, F.J., Ricciardulli, L., Leidner, S.M., Hoffman, R., Atlas, R., 2019. A near-real-time version of the cross-calibrated multiplatform (CCMP) ocean surface wind velocity data set. J. Geophys. Res. Oceans 124, 6997–7010. https://doi.org/10.1029/2019JC015367.

Nguyen, H., Evans, A., Lucas, C., Smith, I., Timbal, B., 2013. The hadley circulation in reanalyses: climatology, variability, and change. J. Clim. 26, 3357–3376. https://doi.org/10.1175/JCLI-D-12-00224.1.

Qiu, B., Chen, S., 2012. Multidecadal sea level and gyre circulation variability in the northwestern tropical Pacific Ocean. J. Phys. Oceanogr. 42, 193–206. https://doi.org/10.1175/JPO-D-11-061.1.

Qiu, B., Chen, S., 2010. Interannual-to-decadal variability in the bifurcation of the north equatorial current off the Philippines. J. Phys. Oceanogr. 40, 2525–2538. https://doi.org/10.1175/2010JPO4462.1.
Qiu, B., Chen, S., Wu, L., Kida, S., 2015. Wind-versus eddy-forced regional sea level trends and variability in the North Pacific ocean. J. Clim. 28, 1561–1577. https://doi.org/10.1175/JCLI-D-14-00479.1.
Qiu, B., Lukas, R., 1996. Seasonal and interannual variability of the North Equatorial Current, the Mindanao Current, and the Kuroshio along the Pacific western boundary. J. Geophys. Res. Oceans 101, 12315–12330. https://doi.org/10.1029/95JC03204.
Qu, T., Kim, Y.Y., Yaremchuk, M., Tuzuka, T., Ishida, A., Yamagata, T., 2004. Can Luzon Strait transport play a role in conveying the impact of ENSO to the South China Sea? J. Clim. 17, 3644–3657. https://doi.org/10.1175/1520-0442(2004)017<3644:CLSTPA>2.0.CO;2.
Saha, S., et al., 2010. The NCEP climate forecast system reanalysis. Bull. Am. Meteorol. Soc. 91, 1015–1057. https://doi.org/10.1175/2010BAMS3001.1.
Stachnik, J.P., Schumacher, C., 2011. A comparison of the Hadley circulation in modern reanalyses. J. Geophys. Res. Atmos. 116 https://doi.org/10.1029/2011JD016677.
Stammer, D., Cazenave, A., Ponte, R.M., Tamisiea, M.E., 2013. Causes for contemporary regional sea level changes. Ann. Rev. Mar. Sci. 5, 21–46. https://doi.org/10.1146/annurev-marine-121211-172406.
Vermeer, M., Rahmstorf, S., 2009. Global sea level linked to global temperature. Proc. Natl. Acad. Sci. USA 106, 21527–21532. https://doi.org/10.1073/pnas.0907765106.
Wang, X., Tong, B., Wang, D., Yang, L., 2020. Variations of the North equatorial current bifurcation and the SSH in the Western Pacific associated with El Niño Flavors. J. Geophys. Res. Oceans 125, 1–16. https://doi.org/10.1029/2019JC015733.
Xiu, P., Chai, F., Shi, L., Xue, H., Chao, Y., 2010. A census of eddy activities in the South China Sea during 1993–2007. J. Geophys. Res. 115, C03012 https://doi.org/10.1029/2009JC005657.
Yaremchuk, M., Qu, T., 2004. Seasonal variability of the large-scale currents near the Coast of the Philippines. J. Phys. Oceanogr. 34, 844–855. https://doi.org/10.1175/1520-0485(2004)034<0844:SVOTLC>2.0.CO;2.
Zebiak, S.E., 1982. A simple atmospheric model of relevance to El Niño. J. Atmos. Sci. 39, 2017–2027. https://doi.org/10.1175/1520-0469(1982)039<2017:ASAMOR>2.0.CO;2.
Zebiak, S.E., Cane, M.A., 1987. A model El Niño–southern oscillation. Mon. Weather Rev. 115, 2262–2278. https://doi.org/10.1175/1520-0493(1987)115<2262:AMENO>2.0.CO;2.
Zheng, Q., Tai, C.-K., Hu, J., Lin, H., Zhang, R.-H., Su, F.-C., Yang, X., 2011. Satellite altimeter observations of nonlinear Rossby eddy–Kuroshio interaction at the Luzon Strait. J. Oceanogr. 67, 365–376. https://doi.org/10.1007/s10872-011-0035-2.